Inorganic Chemistry

Article

pubs.acs.org/IC

^{31}P Magic Angle Spinning NMR Study of Flux-Grown Rare-Earth Element Orthophosphate (Monazite/Xenotime) Solid Solutions: Evidence of Random Cation Distribution from Paramagnetically Shifted NMR Resonances

Aaron C. Palke,*[,†] Jonathan F. Stebbins,[†] and Lynn A. Boatner[‡]

[†]Department of Geological and Environmental Sciences, Stanford University, Stanford, California 94305, United States

[‡]Oak Ridge National Laboratory, Oak Ridge, Tennessee 37831, United States

ABSTRACT: We present ^{31}P magic angle spinning nuclear magnetic resonance spectra of flux-grown solid solutions of $La_{1-x}Ce_xPO_4$ (x between 0.027 and 0.32) having the monoclinic monazite structure, and of $Y_{1-x}M_xPO_4$ (M = V^{n+}, Ce^{3+}, Nd^{3+}, x between 0.001 and 0.014) having the tetragonal zircon structure. Paramagnetically shifted NMR resonances are observed in all samples due to the presence of paramagnetic V^{n+}, Ce^{3+}, and Nd^{3+} in the diamagnetic $LaPO_4$ or YPO_4. As a first-order observation, the number and relative intensities of these peaks are related to the symmetry and structure of the diamagnetic host phase. The presence of paramagnetic shifts allows for increased resolution between NMR resonances for distinct atomic species which leads to the observation of low intensity peaks related to PO_4 species having more than one paramagnetic neighbor two or four atomic bonds away. Through careful analysis of peak areas and comparison with predictions for simple models, it was determined that solid solutions in the systems examined here are characterized by complete disorder (random distribution) of diamagnetic La^{3+} or Y^{3+} with the paramagnetic substitutional species Ce^{3+} and Nd^{3+}. The increased resolution given by the paramagnetic interactions also leads to the observation of splitting of specific resonances in the ^{31}P NMR spectra that may be caused by local, small-scale distortions from the substitution of ions having dissimilar ionic radii.

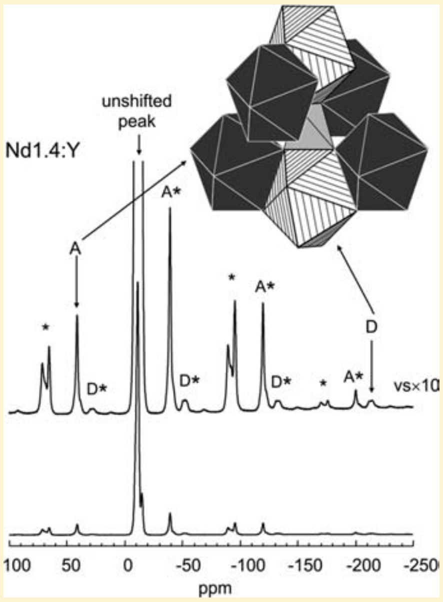

INTRODUCTION

The rare-earth element (REE) orthophosphates monazite and xenotime are accessory minerals in many igneous and metamorphic rocks that have also found important technological applications. Both materials have a formula unit based on REE-PO_4 with monazite being composed primarily of the larger, light REEs (LREE, from La to Gd) whereas the more compact and symmetric structure of xenotime is suited for the smaller, heavy REEs (HREE, from Tb to Lu and Y). In nature, monazite is most commonly dominated by the $CePO_4$ end member with minor amounts of La, Nd, and Gd, whereas xenotime is typically composed primarily of YPO_4. Xenotime crystallizes in the tetragonal zircon structure composed of chains of alternating PO_4 tetrahedra and REE-O_8 polyhedra along the c-axis.[1] The monazite structure can be seen as a lower symmetry (monoclinic) derivative of the zircon structure wherein the LREE are too large for the REE-O_8 polyhedra, and their substitution causes a "shearing" along the c-axis and the creation of larger REE-O_9 polyhedra. Despite the relatively small range in ionic radii [from 0.977 Å (1.117 Å) for Lu^{3+} to 1.16 Å (1.216 Å) for La^{3+} in VIII (IX) coordination[2]] and the similarity between the crystal structures, there is relatively limited solubility between the dominant endmembers, YPO_4 and $CePO_4$. In fact, the temperature dependence of this solubility has been exploited in a number of methods proposed to deduce conditions of chemical equilibrium in rocks containing these minerals ("geothermometers").[3,4] Solubility and distribution of various REE cations (as well as other substituents such as vanadium) in these phases are also important in tailoring their optical properties in a number of technologies such as phosphors and photonic materials. Their ready incorporation of actinides (especially Th and U) and their resistance to radiation damage has led many researchers to suggest their use in long-term sequestration of radioactive waste products.[5−12] The presence of radioactive elements in natural monazite and xenotime has also led to their use as indicators of the age of geologic formations ("geochronology").[13,14]

Solid-state NMR has been widely used to deduce cation distributions and the extent of short-range ordering in many types of oxide materials, relying primarily on changes in isotropic chemical shifts of observed nuclei that are caused by

Received: July 8, 2013
Published: October 16, 2013

ACS Publications

variations in first-shell and more distant cation or anion populations.[15] The application of this method to oxides in which much larger shifts in resonant frequencies can be caused by interactions with unpaired electron spins has been much more limited because, in many cases, peak broadening can be severe, but considerable progress has been made in systems such as the Mn and Fe phosphates and oxyhydroxides of widespread technological and geochemical interest.[16−18]

In principle, this approach can be very sensitive to local structure, as paramagnetic shifts can be orders of magnitude greater than chemical shifts, sometimes allowing small structural variations and the effects of relatively distant neighbors to be detected. The monazite−xenotime phases are an excellent model system in which to explore the incompletely known details of these interactions because of their wide accommodation of different diamagnetic and paramagnetic REE cations, their simple structures, and their distinct symmetries. They also pose important questions about cation order/disorder, which in most models of solid solution is perforce assumed to be random, but for which there are few if any short-range experimental constraints. Early static and magic angle spinning (MAS) NMR studies defined the large "contact shifts" present in paramagnetic phases such as $CePO_4$ and $NdPO_4$.[19,20] However, the substitution of relatively small percentages of paramagnetic cations into the diamagnetic phases YPO_4 and $LaPO_4$ provides an opportunity to test this methodology for determining the details of solution mechanisms, including populations of phosphate groups with varying numbers of substituent neighbors, cation clustering, and "ideality" of mixing. In fact, it is often possible to extract valuable information about short-range order/disorder in inorganic solid solutions from NMR experiments involving paramagnetic species.[21−28] The utility of NMR experiments in obtaining this type of information is usually related to the increase in resolution between distinct atomic configurations when paramagnetically shifted NMR peaks are involved because of the wider range of possible paramagnetic shifts (up to thousands of ppm), whereas ordinary chemical shifts have a much narrower range (e.g., tens to about a hundred ppm).[15]

In our previous study of these materials,[29] a number of solid solutions of the form $La_{1-x}REE_xPO_4$ and $Y_{1-x}REE_xPO_4$, with x between 0.001 and 0.100, were observed by ^{31}P MAS NMR spectroscopy. Paramagnetic substituents included Nd^{3+}, Pr^{3+}, Ce^{3+}, Eu^{3+}, and Dy^{3+}. The work focused on assigning paramagnetically shifted NMR peaks to distinct ^{31}P-REE^{3+} configurations and determining relative contributions from the so-called pseudocontact (through-space) and Fermi contact (through-bond) shift mechanisms. Although the ^{31}P NMR spectra were informative, it was recognized that the samples studied, which were synthesized by powder sintering, were not completely homogeneous solid solutions. In some cases, this led to peak broadening that obscured the resolution and also to the presence of impurity phases. The results presented here extend our previous work by using much more homogeneous flux-grown single crystals with compositions of $La_{1-x}Ce_xPO_4$ and $Y_{1-x}M_xPO_4$ (M = Nd, Ce, and V, with x from 0.001 to 0.32). The enhanced control of the composition and improved spectral resolution in the flux-grown crystals has now allowed us to make refined site assignments and accurate quantization of resonances that can be attributed to phosphate sites with not one but two paramagnetic neighbors, and in less dilute solutions, even three and four neighbors. Through detailed modeling of the expected cation distributions, we show that NMR results for both the monazite and xenotime phases are consistent with random mixing, despite the cation size differences in the latter. Also in xenotime, high-resolution spectra of dilute solutions reveal new details such as peak splitting that may be related to local site distortion caused by the ionic radii mismatch. The present study demonstrates that with a careful analysis of data on high-quality samples, new structural information concerning solid solution mechanisms with paramagnetic end members can be obtained using solid-state NMR.

■ EXPERIMENTAL SECTION

Monazite ($La_{1-x}Ce_xPO_4$) and xenotime ($Y_{1-x}M_xPO_4$, M = V, Nd, and Ce) single crystals were grown by melting the oxide components (V_2O_5, Y_2O_3, La_2O_3, Nd_2O_3, and ,CeO_2) in a $Pb_2P_2O_7$ flux at 1360 °C in a Pt crucible, slowly cooling to 900 °C at a rate of 0.5 to 1 °C/h and then rapidly cooling to room temperature. Crystals were then extracted from the residual flux by boiling the experimental charge in nitric acid for about 1 month. More details of the synthesis method can be found elsewhere.[30,31] Samples were characterized for phase purity by electron probe microanalysis (EPMA) described below and ^{31}P NMR spectroscopy (see the Results and Discussion section). On the basis of these analyses, samples are labeled by host cation and the cation percent of the minor substituent (e.g., Ce1:Y designates $Y_{1-x}Ce_xPO_4$, with $x = 0.01$).

All samples were analyzed on either the JEOL 733 electron microprobe at Stanford University or the Cameca SX-100 at the University of California, Davis, using various materials from phase-pure, flux-grown REE orthophosphates, synthetic REE oxides, to REE-silicides for standards. These results show that, in general, the flux-grown crystals are much more homogeneous than our previously studied powder-sintered samples:[29] uncertainties given in Table 1 reflect the variation among multiple analysis spots as well as instrumental precision. Pb contents were measured in addition to P, V, Y, La, Ce, and Nd. In a few cases, bright spots were detected in backscattered electron images and were found to be inclusions of the $Pb_2P_2O_7$ flux. However, Pb contents were below the limit of detection (about 0.1%) outside of these discrete inclusions. Measured compositions are reported in Table 1 along with those of the starting materials. For the $Y_{1-x}M_xPO_4$ samples, the measured V, Nd, and Ce contents are much lower than the those for the batch compositions due to the size mismatch between the Y^{3+} ion and substituting Nd^{3+}, Ce^{3+}, or any of the likely V^{n+} cations, which resulted in their partitioning into the flux phase. In contrast, measured and batch compositions agree quite well for the $La_{1-x}Ce_xPO_4$ solid solutions because of the closeness in size of La^{3+} and Ce^{3+}.

Table 1. EPMA Results for $La_{1-x}Ce_xPO_4$, $Y_{1-x}RE_xPO_4$, and $Y_{1-x}V_xPO_4$ Samples

$La_{1-x}Ce_xPO_4$	x (batch)	x (EPMA)
Ce3:La	0.03	0.027 (3)
Ce16:La	0.17	0.160 (6)
Ce:22La	0.22	0.220 (6)
Ce32:La	0.33	0.323 (8)
$Y_{1-x}Nd_xPO_4$	x (batch)	x (EPMA)
Nd0.2:Y	0.01	0.0018 (6)
Nd1.4:Y	0.10	0.014 (3)
$Y_{1-x}Ce_xPO_4$	x (batch)	x (EPMA)
Ce0.1:Y	0.01	0.001 (1)
Ce0.5:Y	0.10	0.005 (1)
Ce1:Y	0.20	0.010 (1)
$Y_{1-x}V_xPO_4$	x (batch)	x (EPMA)
V0.2:Y	0.06	0.002 (1)

Table 2. Measured Intensities of Peaks Seen in $Y_{1-x}Nd_xPO_4$ and $Y_{1-x}V_xPO_4$ Samples

	Nd0.2:Y			Nd1.4:Y				V0.2:Y		
	shift (ppm)[a]	area	model	shift (ppm)[a]	predicted shift (ppm)	area	model		shift (ppm)[a]	area
US	0	95 (1)	97.236	0		75 (4)	82.087			
singly shifted peaks								US	0	90 (2)
A	52.3 (5)	0.8 (1)	0.767	52.5 (5)		3.7 (7)	4.165	paramagnetically shifted peaks		
B	2.2 (2)	1.1 (3)	0.767	2.4 (2)		5 (1)	4.165	A	19.5 (5)	0.4 (1)
C	−3.8 (2)	1.0 (2)	0.767	−3.6 (2)		4 (1)	4.165	B	12.7 (5)	0.6 (1)
D1	−201.3 (5)	0.23 (6)		−200.8 (5)		1.2 (3)		C	8.8 (5)	0.3 (1)
D2	−203.5 (5)	0.20 (6)		−203.9 (5)		1.0 (2)		D	5.0 (5)	1.0 (2)
sum of D1 + D2		0.4 (1)	0.384			2.2 (5)	2.082	E	2.4 (3)	1.9 (6)
E	0.8 (2)	0.9 (3)	0.767	1.0 (2)		4 (1)	4.165	F	−1.9 (3)	3 (1)
F	−0.5 (2)	0.8 (3)	0.767	−0.5 (2)		5 (1)	4.165	G	−5.1 (5)	1.2 (4)
doubly shifted peaks								H	−8.3 (5)	0.6 (2)
AB			0.006	54.5 (5)	54.9	0.4 (1)	0.384	I	−13.1 (5)	0.6 (2)
AC			0.006	49.8 (5)	48.9	0.4 (1)	0.384			

[a] Shifts are calculated as the difference in position from the main unshifted peak (US) at −11.4 ppm from a spectrum collected without heating the sample (approximately 46 °C with frictional heating of spinning rotor).

Table 3. Measured Intensities of Peaks Seen in $Y_{1-x}Ce_xPO_4$ Samples[a]

	Ce0.1:Y				Ce0.5:Y				Ce1:Y			
	shift (ppm)[b]	predicted shift (ppm)	area	model	shift (ppm)[b]	predicted shift (ppm)	area	model	shift (ppm)[b]	predicted shift (ppm)	area	model
US	0		97.8 (5)	98.61	0		93.5 (5)	93.2	0		86 (1)	86.9
singly shifted peaks												
A	18.8 (5)		0.41 (4)	0.39	18.8 (5)		2.0 (3)	1.9	18.8 (5)		3.7 (4)	3.5
B	0.6 (2)		0.39 (4)	0.39	0.5 (2)		1.5 (3)	1.9	0.5 (2)		3.5 (5)	3.5
C	−0.6 (2)		0.37 (4)	0.39	−0.6 (2)		1.6 (3)	1.9	−0.6 (2)		3.7 (9)	3.5
D	−43.6 (5)		0.18 (3)	0.20	−43.6 (5)		1.0 (2)	0.9	−43.6 (5)		1.7 (2)	1.8
doubly shifted peaks												
AB				0.002	21.7 (5)	19.3	0.05 (2)	0.04	21.7 (5)	19.3	0.19 (3)	0.14
AC				0.002	14.3 (5)	18.2	0.07 (3)	0.04	14.3 (5)	18.2	0.13 (3)	0.14
DB				0.001	−42.5 (5)	−43.1	0.06 (3)	0.02	−41.8 (5)	−43.1	0.2 (1)	0.07
DF				0.001	−45.9 (5)	−44.2	0.04 (2)	0.02	−45.0 (5)	−44.2	0.13 (4)	0.07
DC				0.001	−49.0 (5)		0.05 (3)	0.02	−49.0 (5)		0.2 (1)	0.07
AD1					−21.95 (5)		0.009 (3)		−21.6 (5)		0.03 (1)	
AD2					−28.66 (5)		0.008 (3)		−28.52 (5)		0.03 (1)	
AD3					−31.15 (5)		0.006 (2)		−30.84 (5)		0.04 (1)	
sum of AD1,2,3				0.001	−27.3	−24.8	0.023 (8)	0.019	−27.0	−24.8	0.10 (3)	0.07
prediction for triply shifted peaks												
including D				0.000				0.000				0.003
not including D				0.000				0.001				0.006

[a] Predictions based on a random distribution model for singly, doubly, and triply paramagnetically shifted peaks are included as well for comparison. [b] Shifts are calculated as the difference in position from the main unshifted peak (US) at −11.4 ppm from a spectrum collected without heating the sample (approximately 46 °C with frictional heating of spinning rotor).

^{31}P MAS NMR spectra were collected on powdered samples with a Varian Infinity-Plus 400 spectrometer at 9.4 T (161.8 MHz for ^{31}P) using Varian/Chemagnetics "T3"-type probes. A probe with 3.2 mm rotors was used when higher spinning speeds (to 22 kHz) were needed; variation in air frictional heating with spinning rate allowed temperature to be varied by up to 35 °C, which was useful in confirming paramagnetically shifted resonances. A probe with 4 mm rotors (to 14 kHz) was employed to improve signal-to-noise ratios with larger samples and for controlled variable temperature (VT) studies up to 162 °C. Temperatures were calibrated with the ^{207}Pb resonance of $Pb(NO_3)_2$.[32] Radio frequency tip angles of about 15° were used for both probes, and spectra were referenced to $NH_4H_2PO_4$ at 0.8 ppm with reference to 85% aqueous H_3PO_4 at 0 ppm. Pulse delays varied from 0.05 to 5200 s to obtain different types of information for each sample. Shorter pulse delays were used to emphasize and quantify the quickly relaxing paramagnetically shifted peaks, whereas much longer delays were needed to obtain fully relaxed spectra that allowed for accurate measurement of the unshifted resonances without nearby paramagnetic neighbors and long relaxation times. Note that from here on the term "unshifted peak" will refer to a resonance that does not experience a frequency change due to nearby paramagnetic neighbors and thus has the same peak position as the pure diamagnetic endmember phase. These positions do, of course, include the standard chemical shifts, which are listed in Tables 2 and 3. The term "paramagnetically shifted peak" will be used to describe a resonance that has been shifted away from the unshifted peak due to an interaction with a nearby paramagnetic cation. The magic angle was set to within 0.1° by optimizing the ^{79}Br rotational echo train for powdered KBr.[33] This was found to be particularly important to avoid the production of unusual, low-intensity features in spectra of paramagnetic materials where peaks may potentially have significantly anisotropic chemical shifts or paramagnetic shift tensors.

Peak areas were determined by fitting with the program DMFIT.[34] The paramagnetic shift anisotropy varies considerably between different peaks necessitating inclusion of the spinning sideband areas to the total intensities of the isotropic resonances. The best fits to the peaks were obtained using 80% Gaussian/20% Lorentzian line shapes. When possible, line widths within a spectrum were allowed to vary independently and typically converged on very similar values. However, in some cases when peaks became too broad or overlapped significantly, an optimal mean width was determined visually and was fixed for all peaks during the deconvolution.

No attempt was made to measure the spin−lattice relaxation times for the various paramagnetically shifted peaks in the samples studied herein. These data could help refine the peak assignment models developed in this study due to the proposed dependence of spin−lattice relaxation times on $1/r^6$, where r is the distance between the resonating nucleus and the paramagnetic cation. However, given the fact that most of the paramagnetically shifted peaks are fully relaxed in single pulse spectra collected with a pulse recycle delay of 0.05 s, spin−lattice relaxation times are likely to be small and challenging to measure precisely. Future studies could potentially benefit from such measurements.

RESULTS AND DISCUSSION

$La_{1-x}Ce_xPO_4$ Monazite Solid Solutions. The ^{31}P NMR spectra collected at varying rotor spinning speeds (to give slightly different sample temperatures) of the flux-grown sample Ce3:La with 3% Ce are shown in Figure 1. A comparison with the spectra collected from a sintered sample of composition $La_{0.90}Ce_{0.10}PO_4$ from our previous study[29] shows that, except for the absence of the unidentified impurity phase at −27.1 ppm from the flux-grown sample and the decreased peak broadening due to the lower concentration of Ce^{3+}, the spectra are very similar. The increase in resolution due to the narrowing of the peaks in the new samples leads us to slightly alter the peak assignment given previously. The resonance at −21.5 ppm in the previous study was thought to be one peak and was assigned to one specific $^{31}P-Ce^{3+}$ interaction; however, the asymmetry of this peak in the spectrum of flux-grown Ce3:La, collected at a spinning speed of 14 kHz, makes it clear that this resonance band actually contains contributions from two distinct peaks (D and E). When the rotor spinning speed was increased to 22 kHz, raising the sample temperature by about 35 °C, the resolution between the two peaks was blurred as their paramagnetic shifts decreased and they moved in toward the main unshifted peak with all La neighbors at −4.4 ppm. Therefore, we can now identify seven distinct paramagnetically shifted peaks (A through G) and assign these to each of the seven unique $^{31}P-Ce^{3+}$ configurations possible when considering next-nearest neighbor interactions only (i.e., there are seven La^{3+} sites in the first shell of a PO_4 tetrahedron into which Ce^{3+} can substitute, each with distinct bond distances and angles). Given this peak assignment, each of the paramagnetically shifted peaks should have an equal intensity because they are caused by configurations that occur equally frequently from the perspective of the ^{31}P nucleus: there are no crystallographic distinctions among these configurations and thus no reason for any preference for isolated substitutions. Fitting of the spectra of Ce3:La shows that this is the case with each paramagnetically shifted peak constituting 2.5 (4) % of the total intensity, further corroborating our peak assignment model. The paramagnetic interactions caused by two of these $^{31}P-Ce^{3+}$ configurations produce shifts to positive frequencies (relative to the unshifted peak for P with all La neighbors), whereas the other five impart negative shifts. This is in contrast to the paramagnetic shifts seen in $La_{0.96}Nd_{0.04}PO_4$, where seven paramagnetically shifted peaks were observed, but three are shifted to more positive frequencies and four to lower frequencies.[29] This difference in behavior is likely the result of varying contributions from the pseudocontact (through-space) and the Fermi contact (through-bond) shifts for Ce^{3+} vs Nd^{3+}. Both of these effects can be positive or negative, and therefore, a change in the relative contribution of a negative pseudocontact shift and a positive Fermi contact shift (or vice versa) could easily change the overall sign of the observed paramagnetic shift.

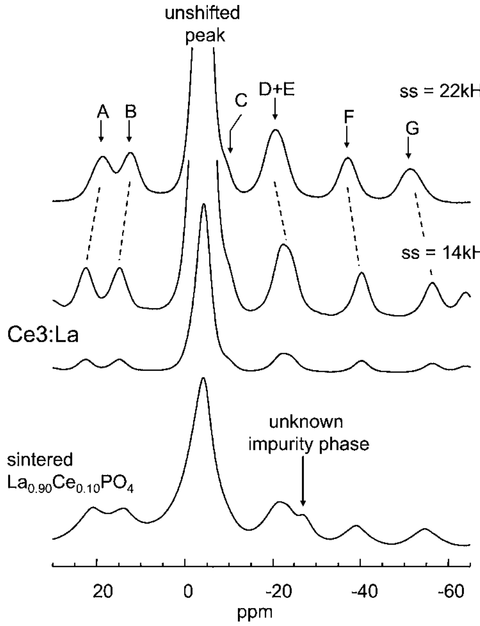

Figure 1. ^{31}P MAS NMR spectra (9.4 T) of flux-grown Ce3:La ($La_{0.97}Ce_{0.03}PO_4$) collected with spinning speeds of 14 and 22 kHz and 0.05 s pulse delays. The upper two spectra are enlarged 4× relative to the lower spectrum. A through F mark paramagnetically shifted peaks, and the position of the unshifted peak for phosphate groups with no close Ce^{3+} neighbors is labeled as well. Dashed lines show the change in peak positions with the temperature changes caused by varying spinning speeds (about 35 °C). The lowermost spectrum is of a sintered sample ($La_{0.90}Ce_{0.10}PO_4$) shown for comparison.[29]

The ^{31}P NMR spectra of flux-grown $La_{1-x}Ce_xPO_4$ samples with progressively higher concentrations of Ce^{3+} (Ce16:La and Ce32:La) were collected to determine the effects of high levels of paramagnetic species and how their interactions affect the information that can be obtained about solid solution mechanisms in such systems (uppermost spectra in Figure 2). Here, rotor spinning speeds up to 22 kHz were needed to avoid excessive overlap of sidebands (not shown in the figures) and isotropic peaks. The first attempts to fit the spectra of Ce16:La and Ce32:La were made using the main unshifted peak at −4.4 ppm and the positions of the seven shifted peaks A through G, as seen in the spectrum for Ce3:La, as constraints. It was found that by using these eight peaks, and allowing only their widths to vary, reasonably good fits could be obtained. However, the resulting peak areas were found to be significantly unequal, and their fitted intensities were substantially greater than predicted by a random distribution of Ce^{3+}. Therefore, a more complete model was developed that included peak intensities for sites with more than one paramagnetic neighbor, as given for a random distribution by the binomial distribution:

$$I_k = mx^k(1 - x)^{n-k} \quad (1)$$

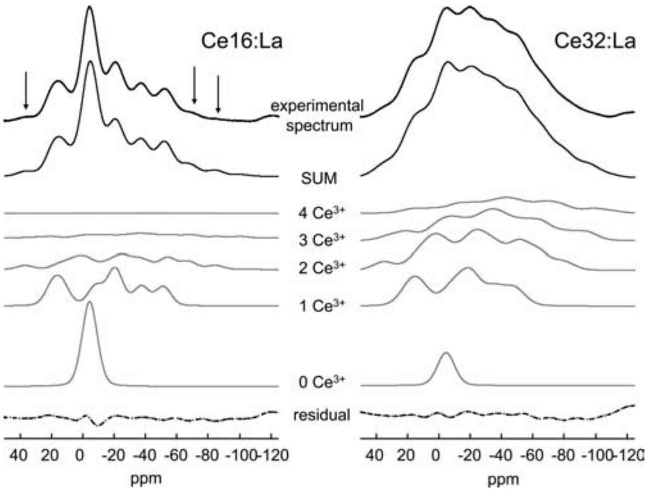

Figure 2. Results of spectral modeling for Ce16:La and Ce32:La ($La_{1-x}Ce_xPO_4$, $x = 0.16$ and 0.32, respectively) as described in the text. Lighter colored spectra show contributions from ^{31}P nuclei having zero, one, two, three, and four first-shell Ce^{3+} neighbors, and the sum of these is shown immediately above. The experimental ^{31}P NMR spectra of Ce16:La and Ce32:La collected with a spinning speed of 22 kHz and 0.05 s pulse delays are shown as well; the residual between the experimental and simulated spectra are shown as the dashed lines at the bottom. The peaks related to PO_4 groups having more than one first-shell Ce^{3+} neighbor at +36, −69, and −85 ppm are marked by arrows as mentioned in the text.

where m is the number of configurations that can give rise to a specific peak (equal to 1 here but 2 or 4 for the $Y_{1-x}M_xPO_4$ samples described below), k is the number of Ce^{3+} interacting with the ^{31}P nucleus for the specific peak, n is the total number of sites into which Ce^{3+} can enter and cause a specific paramagnetically shifted peak (equal to 7 here for the 7 distinct first-shell $^{31}P{-}Ce^{3+}$ configurations), and x is the probability of Ce^{3+} occupying an REE-O_9 site and is equal to the concentration of Ce^{3+} (out of total Ce + Y). At higher Ce^{3+} concentrations, contributions from ^{31}P nuclei with more than one Ce^{3+} neighbor in their first shell become important. The number of possible doubly ($k = 2$), triply ($k = 3$), or quadruply shifted ($k = 4$) peaks is given by

$$N_k = \frac{n!}{k!(n-k)!} \tag{2}$$

The total intensity of all doubly, triply, or quadruply shifted peaks can be calculated by multiplying this number (N_k) by the intensity of the peak (I_k) given by eq 1. For Ce16:La, the total fractions of ^{31}P nuclei having one, two, three, or four Ce^{3+} neighbors are 39%, 24%, 8%, and 2%, respectively, and for Ce32:La these are 21%, 31%, 25%, and 12%. It is thus apparent that modeling the spectra with only one unshifted main peak at −4.4 ppm and seven peaks for ^{31}P having only one first-shell Ce^{3+} neighbor is insufficient. Equation 2 shows that the development of a more complete model would require 1, 7, 21, 35, and 35 peaks (99 total) for ^{31}P nuclei with zero, one, two, three, and four first-shell Ce^{3+} neighbors respectively. Although it would be nearly impossible to implement such a model with a least-squares regression calculation having independently varying peak intensities, if good estimates for peak positions for the multiply shifted peaks were available, it would be possible to produce a "synthetic" spectrum with the intensities of these peaks constrained by the intensities predicted above. This synthetic spectrum could then be compared to the experimental data, and the validity of the assumption of random distribution of Ce^{3+} could be tested. It is generally accepted that, as a first approximation, paramagnetic shifts are additive.[35,36] Therefore, peak positions for ^{31}P having two, three, or four Ce^{3+} neighbors can be estimated by determining the possible combinations of peaks A through G (i.e., AB, AC, ..., AG, BC, BD, ..., BCG, BDE, etc.) and calculating the peak positions by adding the paramagnetic shifts of the singly shifted peaks involved, as determined from the spectra of the dilute solid solution. In this model, ^{31}P nuclei having five or more first-shell Ce^{3+} neighbors would contribute less than 1% of the total signal for Ce16:La and less than 4% for Ce32:La, and were thus left out for simplicity. The main adjustable variables are peak widths, which were set at 11.5 and 16 ppm for Ce16:La and Ce32:La, respectively. The results of this modeling for Ce16:La and Ce32:La are shown in Figure 2, which gives the sum of all peaks as well as the separate contributions for the singly, doubly, triply, and quadruply shifted peaks. The model spectra match the experimental data remarkably well, lending credence to the assumption of a random distribution of La^{3+} and Ce^{3+} in these $La_{1-x}Ce_xPO_4$ solid solutions over a wide compositional range. Besides the overall closeness of the fit to experimental data, our model spectra quite accurately predict features seen in the spectra of the higher Ce^{3+} samples. Note, for instance, the low-intensity peaks at +36, −69, and −85 ppm (marked by arrows in Figure 2) present in samples with x = 0.16 and 0.32 but not Ce3:La. It is evident that these low-intensity peaks cannot be described using only unshifted and singly shifted peaks but are well described by the doubly or triply shifted peaks in our model. Minor deviations between the model and experimental data are expected due to our inability to accurately model spinning sidebands. These discrepancies are expected to be small, because even at the highest Ce^{3+} concentrations, most of the experimental intensity is in the isotropic peaks and the overall shape of the sideband manifolds (not shown in the figures) is not significantly different from the band of isotropic resonances.

One important trend in the data is a shift in the center of gravity of the band of isotropic resonances to lower frequencies with increasing Ce^{3+} concentration. This is expected, as the resonances for $La_{1-x}Ce_xPO_4$ solid solutions should bridge the gap between the peak for pure $LaPO_4$ at −4.4 ppm and that of $CePO_4$ at −90 ppm.[19,20,29] We also note that, at least in this system, the development of a host of overlapping resonances with varying paramagnetic shifts is the major contribution to the overall line broadening at higher dopant concentrations, rather than a severe shortening of relaxation times.

$Y_{1-x}Nd_xPO_4$ Xenotime Solid Solutions. The ^{31}P NMR spectra of flux-grown $Y_{1-x}Nd_xPO_4$ samples Nd0.2:Y and Nd1.4:Y (Table 1) are presented in Figure 3. The main features are very similar to those seen in the powder-sintered samples with one main unshifted peak at −11.4 ppm corresponding to PO_4 tetrahedra with only Y neighbors and two paramagnetically shifted peaks at +41.0 ppm (A) and −214.0 ppm (D) with relative integrated intensities of 2:1.[29] This ratio led to the assignment of these peaks to ^{31}P nuclei with paramagnetic Nd^{3+} in a corner-shared site at 3.763 Å (A) and an edge-shared site at 3.014 Å (D), as these correspond to the number of times each of these specific $^{31}P{-}Nd^{3+}$ configurations occur around each phosphate site.[1,29] This aspect of the structure is also shown in Figure 3. Here, peak A corresponds to ^{31}P having Nd^{3+} in the solid-shaded, corner-

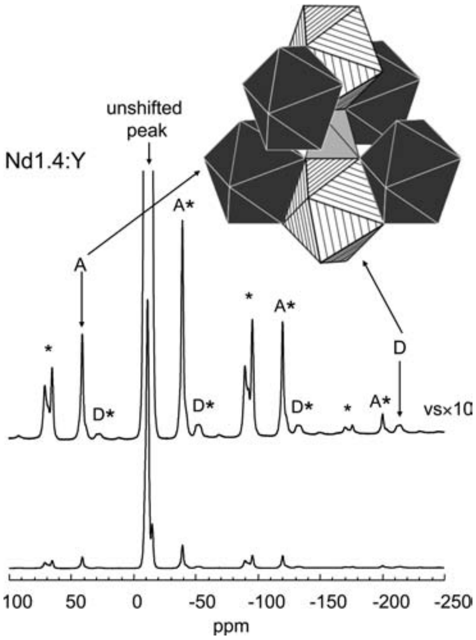

Figure 3. ^{31}P MAS NMR spectrum of Nd1.4:Y ($Y_{1-x}Nd_xPO_4$, x = 0.014) collected with a spinning speed of 13 kHz and 1 s pulse delay. Sidebands of peaks A, D, and the cluster of peaks around −11 ppm are shown by A*, D*, and *, respectively. The inset shows the structure around a PO_4 tetrahedron: the edge-shared sites assigned to peak D are striped, and the corner-shared sites (peak A) are dark gray.

shared polyhedra and peak D to the striped, edge-shared polyhedra. Although a thorough analysis and assignment of paramagnetic shifts to specific Fermi contact shift mechanisms (bond polarization or through-bond unpaired electron spin delocalization) is outside of the scope of this study, it should be noted that the difference in sign and magnitude of the shifts for peaks A and D correlate well with the change in P−O−Nd bond angles (155.2° and 98.2°, respectively) for our peak assignment model. This correlation qualitatively agrees with theoretical analyses of previous researchers.[37−42]

Peaks B and C, seen in the previous study,[29] also appear in the spectra of the flux-grown samples, at −9.1 and −13.2 ppm (Figure 4). The near equivalence of the integrals of B and C to that of A, and their small paramagnetic shifts, suggested that they are caused by a pseudocontact shift mechanism involving $^{31}P-Nd^{3+}$ configurations in the cation coordination shells at 4.876 and 5.685 Å, as there are two distinct types of these configurations, each with four equivalent sites.[1,29] These two $^{31}P-Nd^{3+}$ configurations are shown as the striped and solid dark gray polyhedra in the inset of Figure 4. In expanded portions of the spectra centered on peak A (Figure 4), two shoulders are present at +43.1 and +37.8 ppm, labeled AB and AC, respectively. These are seen for Nd1.4:Y but not for Nd0.2:Y and thus appear only as the Nd concentration increases. The structure around peak A for the higher Nd sample closely resembles that around the main, unshifted peak, which has B and C as shoulders. AB and B are shifted +2 ppm from A and the unshifted resonance, respectively, whereas AC and C are each shifted by −3 ppm. The similarity of these patterns leads to the assignment of peaks AB and AC as ^{31}P nuclei having two Nd^{3+} neighbors: one Nd^{3+} in a nearby corner-shared site and one Nd^{3+} in one of the more distant sites giving rise to peaks B or C respectively.

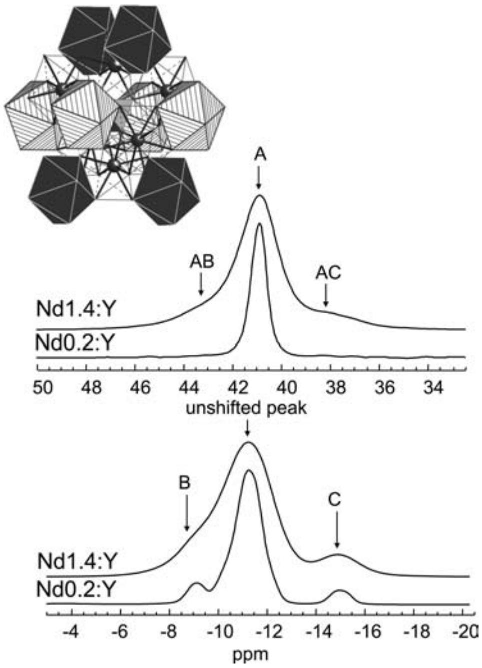

Figure 4. ^{31}P MAS NMR spectra of Nd1.4:Y and Nd0.2:Y ($Y_{1-x}Nd_xPO_4$, x = 0.014 and 0.002, respectively) collected with a spinning speed of 14 kHz and pulse delays of 0.05 s. The bottom two spectra from samples with x = 0.014 and x = 0.002 are centered on the unshifted peak and show singly shifted peaks B and C. The top two spectra from the same samples are centered on peak A showing doubly shifted peaks AB and AC. Spectra are normalized to the most intense peak in the frequency range shown. The inset shows an expanded view of the structure around a PO_4 tetrahedron. There are two distinct sites shown where Nd^{3+} can occur, which are presumed to be related to peaks B and C. The striped polyhedra are at a distance of 4.876 Å from P and the dark gray polyhedra at 5.685 Å. The YO_8 sites related to peaks A and D (Figure 3) are shown here as ball and stick polyhedra.

Closer inspection of peak D in the $Y_{1-x}Nd_xPO_4$ xenotimes shows an obvious splitting into two roughly equal components labeled D1 and D2 in Figure 5. The relative integrated intensities of A, D1, and D2 (Table 2) again suggests that both

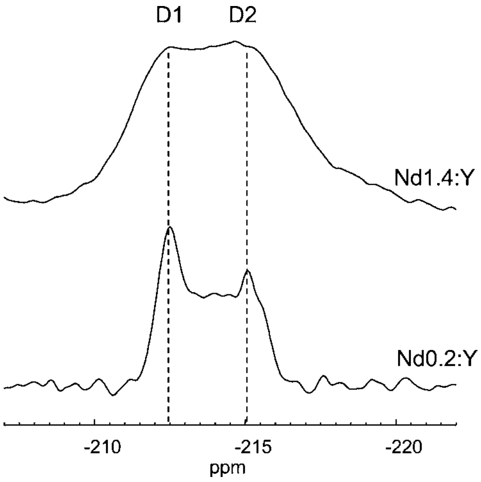

Figure 5. ^{31}P MAS NMR spectra of Nd1.4:Y and Nd0.2:Y ($Y_{1-x}Nd_xPO_4$, x = 0.014 and 0.002, respectively) collected with a spinning speed of 14 kHz and pulse delays of 0.05 s, centered on peak D. Spectra are normalized to the maximum peak intensity.

D1 and D2 are related to edge-shared $^{31}P-Nd^{3+}$ configurations, because the intensity of D1 + D2 is half that of A, and the concentrations of Nd^{3+} estimated from the intensities of the paramagnetic shift using this peak model agree well with the EPMA data. As mentioned above, solid solutions between members of the tetragonal HREE-PO_4 xenotime group and the monoclinic LREE-PO_4 monazite group are limited due to the size mismatch in ionic radii between the LREE and HREE groups. The significant difference in the ionic radii of Nd^{3+} (1.109 Å) and Y^{3+} (1.019 Å)[2] may also help explain the splitting of peak D if the substitution of Nd^{3+} for Y^{3+} is accompanied by a significant structural distortion. If such a distortion is large enough to locally lower the symmetry of the $REEO_8$ site occupied by Nd^{3+} from, for example, D_{2d} to C_{2v}, this could cause $^{31}P-Nd^{3+}$ configurations corresponding to the two first-shell edge-shared sites and their associated paramagnetic shifts to become nonequivalent. It is thus possible that small symmetry-lowering structural distortions could cause the observed small degree of peak splitting (about 2 ppm out of 200 ppm total shift). For comparison, we note that variations in distances and bond angles in the $^{31}P-Nd^{3+}$ configurations for the Nd-doped xenotime samples from 3.014 to 3.762 Å and 98.2 to 155.2°, respectively[1] produce a range of paramagnetic shifts of 255 ppm from +41.0 to −214.0 ppm. This wide range of paramagnetic shifts suggests that relatively minor deviations from ideal bond lengths and angles in these Nd-doped xenotimes could also produce a measurable effect on the order of the splitting of peaks D1 and D2. Any such symmetry-lowering structural distortion should, in principle, also affect the $^{31}P-Nd^{3+}$ corner-shared configurations corresponding to peak A. However, the nature of this potential structural distortion is not clear, and it is possible that any peak splitting associated with corner-shared $^{31}P-Nd^{3+}$ configurations is simply too small to be observed. Because the corner-shared sites are farther away from the ^{31}P nucleus, and therefore cause smaller paramagnetic shifts, it is also likely that the splitting of peak A will be smaller than that of D. Note also that the splitting of peak D is present in both Nd0.2:Y and Nd1.4:Y and is, therefore, not related to any concentration-dependent processes as are the doubly shifted peaks.

Table 2 shows the areas of these peaks measured by fitting of the $Y_{1-x}Nd_xPO_4$ spectra along with predicted intensities given by a binomial distribution, assuming randomly distributed Nd^{3+} as described above. There is close agreement for the singly shifted peaks A and D1 + D2 and the doubly shifted peaks AB and AC (for sample Nd1.4:Y) with this model (Table 2). Additionally, the binomial distributions also predict that at very dilute concentrations, such as that of Nd0.2:Y, the intensities of doubly shifted peaks should be well below the detection limit of our experiments (about 0.1% of total integrated intensity) (Table 2), further corroborating our peak assignments.

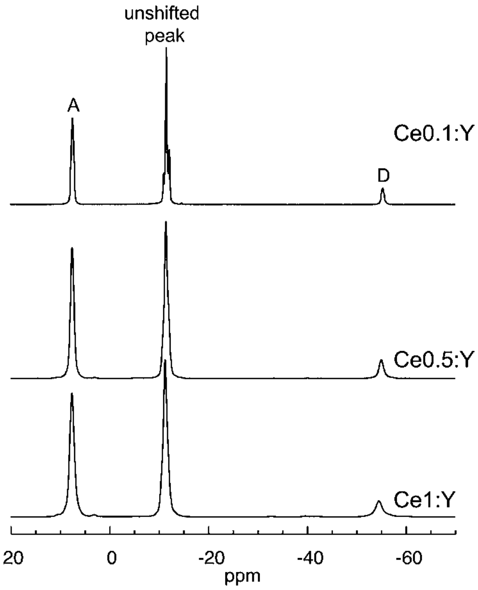

Figure 6. ^{31}P MAS NMR spectra of Ce0.1:Y, Ce0.5:Y, and Ce1:Y ($Y_{1-x}Ce_xPO_4$, $x = 0.001$, 0.005, and 0.010, respectively) collected with pulse delays of 0.05 s.

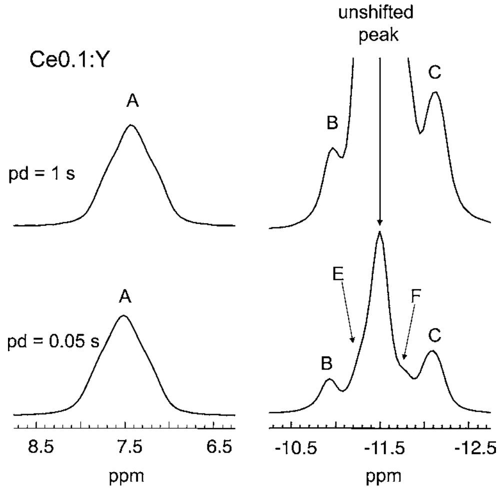

Figure 7. ^{31}P MAS NMR spectra of Ce0.1:Y ($Y_{1-x}Ce_xPO_4$, $x = 0.001$) showing enlarged regions of the spectra for peak A and that close to the main unshifted peak. The bottom spectra were collected with a pulse delay of 0.05 s, and the top spectra were collected with a pulse delay of 1 s. Spectra are normalized to the intensity of peak A for each delay time.

$Y_{1-x}Ce_xPO_4$ Xenotime Solid Solutions. As with the materials described above, the main features of the ^{31}P NMR spectra for the flux-grown $Y_{1-x}Ce_xPO_4$ crystals Ce0.1:Y, Ce0.5:Y, and Ce1:Y (Table 1) are the same as in the powder-sintered samples,[29] with one main peak at −11.4 ppm corresponding to the unshifted resonance of ^{31}P with all Y neighbors and paramagnetically shifted peaks at +7.5 ppm (A) and −54.7 ppm (D) (Figure 6). It is interesting to note the much smaller magnitude of the paramagnetic shifts when Ce^{3+} substitutes into the YPO_4 lattice as opposed to Nd^{3+}. As described in our previous study, the magnitudes of these shifts correlate well with the resonances of the pure paramagnetic orthophosphate phases ($CePO_4$ at −90 ppm and $NdPO_4$ at −251 ppm), which, again, correlate well with the magnetic susceptibility of these materials.[29] In the two low-Ce^{3+} samples, two additional paramagnetically shifted peaks are seen flanking the main peak at −10.9 ppm (B) and −12.1 ppm (C) (Figure 7). Peaks B and C were not observed previously in powder-sintered $Y_{1-x}Ce_xPO_4$.[29] It is evident here that when very short pulse delays are used, peaks B and C have significantly less intensity than peak A, which seems to preclude the application of the peak assignment model developed for the $Y_{1-x}Nd_xPO_4$ samples above. However, when a 1 s pulse delay is employed (Figure 7), it is seen that peaks B and C increase in intensity relative to peak A. Although peaks B and C are narrower than peak A, when each peak is integrated with its sideband contributions, their intensities are very close to equal. Although it is initially surprising that peaks B and C would have relaxation times significantly longer than peak A (as all are paramagnetically shifted), this finding actually further bolsters our peak assignments, because the relaxation time is expected to vary with $1/r^6$, where r is the distance between the resonating nucleus and the paramagnetic center.[43] Therefore, it is likely that peaks B and C were not observed in the sintered samples[29] due to their long relaxation times combined with overall increased peak broadening. Our model, therefore, is consistent with that of the Nd-xenotimes above with peaks A and D related to the presence of Ce^{3+} in the corner- and edge-shared sites at 3.763 and 3.014 Å (see inset of Figure 3), respectively, and peaks B and C corresponding to Ce^{3+} in the cation coordination shells at 4.876 and 5.685 Å (see inset of Figure 4). Furthermore, the spectra of the two low Ce^{3+} samples show evidence of two additional peaks even closer to the main unshifted peak, labeled E and F in Figure 7. Due to their small shifts and their prominence in even the sample with the lowest Ce^{3+} concentration, we conclude that peaks E and F are caused by third-shell $^{31}P-Ce^{3+}$ configurations at or beyond 7.525 Å.

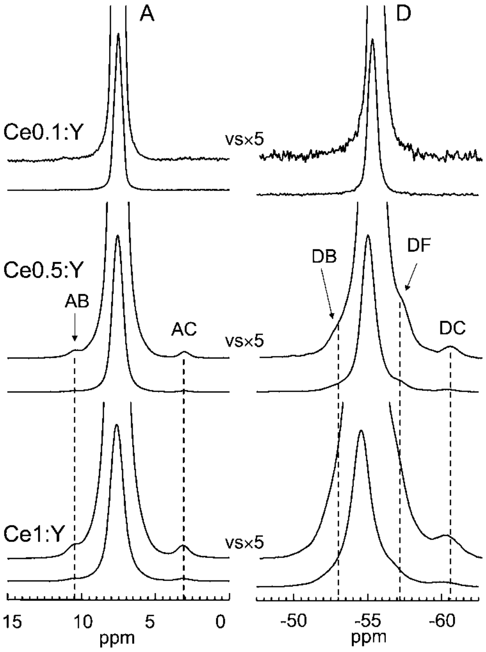

Figure 8. ^{31}P MAS NMR spectra of Ce0.1:Y, Ce0.5:Y, and Ce1:Y ($Y_{1-x}Ce_xPO_4$, x = 0.001, 0.005, and 0.010, respectively) collected with pulse delays of 0.05 s, showing expanded regions for peaks A and D. Doubly shifted peaks are labeled as in the text. For each sample, the lower spectrum is normalized to the intensity of the main peak and is overlaid with the same region with a vertical scale expanded 5×.

Figure 8 presents the fine structure in the vicinity of paramagnetically shifted peaks A and D and how this changes with increasing Ce^{3+} concentration. At the lowest concentration, only peaks A and D themselves are detectable. However, with higher Ce^{3+}, additional resonances appear around both peaks A and D. Their intensities increase with increasing Ce^{3+}, indicating that these are double shifts caused by interaction of ^{31}P with two Ce^{3+} neighbors. There are two such features flanking peak A at +10.5 ppm (AB) and +3.1 ppm (AC) that are shifted +3.0 ppm and −4.4 ppm from peak A, respectively. There are three more doubly shifted peaks around D at −53.0 (DB), −57.2 (DF), and −60.4 ppm (DC) that are shifted +1.7, −2.5, and −5.7 ppm, respectively. Unlike the approximation made (by necessity) in our model for the Ce-monazites, these peaks have shifts that are clearly not exact sums of the individual shifts for single paramagnetic neighbors in the corresponding configurations. In fact, the shift increments of these doubly shifted peaks from A and D are significantly greater than the shifts of peaks B, C, and F (+0.5, −0.7, −0.3 ppm, respectively). However, we are confident in these assignments considering the growth of the intensities of these peaks with the concentration of Ce^{3+} and the close similarity in the numbers and geometry of these shoulders around A and D with those for the main unshifted resonance. It is possible that the first approximation of linear paramagnetic shift additivity is not always the rule and that magnetic or structural interactions between two spatially related Ce^{3+} ions may slightly alter the paramagnetic shift experienced by the ^{31}P nuclei with two such neighbors.

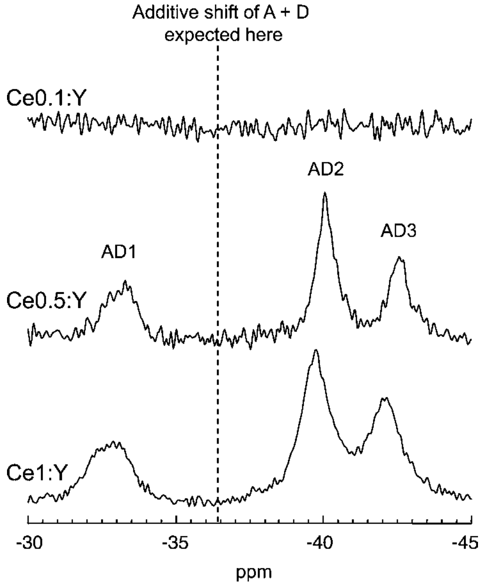

Figure 9. ^{31}P MAS NMR spectra of Ce0.1:Y, Ce0.5:Y, and Ce1:Y ($Y_{1-x}Ce_xPO_4$, x = 0.001, 0.005, and 0.010, respectively) collected with pulse delays of 0.05 s, showing the region where doubly shifted peak AD is expected. The lower two spectra are normalized to maximum peak intensity, whereas the upper spectrum is enlarged to show the absence of detectable features. The expected location of AD, assuming additive shifts and no local distortion, is shown by the dashed line.

In the ^{31}P NMR spectra of the powder-sintered $Y_{1-x}Ce_xPO_4$ samples, two peaks were observed at −41.8 and −34.0 ppm.[29] These materials were demonstrably heterogeneous and spectral resolution was reduced and peak fitting was hampered by the presence of a broad resonance for unreacted, pure phase $CePO_4$.[29] In this area of the spectra of the flux-grown samples (Figure 9), we observe three distinct peaks at −32.9 ppm (AD1), −39.9 ppm (AD2), and −42.7 ppm (AD3). As a first approximation, only one doubly shifted peak AD is expected at about −36 ppm. We now suspect that all three peaks in this region are the result of splitting of the AD resonance by structural distortion caused by the size mismatch between Y^{3+} (1.019 Å) and Ce^{3+} (1.143 Å)[2], as noted above for the Nd-xenotime case. This conclusion is supported by the fact that the sum of the integrated intensities of these three peaks closely matches the predicted intensity of the doubly shifted AD resonances in both Ce0.5:Y and Ce1:Y (Table 3). An examination of the YPO_4 crystal structure presents at least one way in which combinations of edge- and corner-shared $^{31}P{-}Ce^{3+}$ configurations could produce more than one peak. If a ^{31}P nucleus has one corner-shared Ce^{3+} neighbor, an edge-shared Ce^{3+} can occupy the site either nearer to or farther from the corner-shared neighbor at distances of 3.762 and 5.685 Å, respectively. If magnetic interactions between Ce^{3+} ions or structural distortions cause variations from strict additivity of the paramagnetic shifts, then these two configurations could produce two different peaks. There are four ways in which each ^{31}P nucleus can have either of these two configurations. It is possible that if the Ce^{3+} substitution sufficiently distorts the Y^{3+} site such that the symmetry is significantly lowered, then the peaks caused by the two configurations described above could be split even further. However, on the basis of the arguments presented above, we tentatively assign the peaks between −30 and −45 ppm to ^{31}P nuclei having two Ce^{3+} neighbors in some combination of edge- and corner-shared sites with magnetic interactions between the Ce^{3+} ions and/or strong local structural distortion causing splitting of the single peak expected for this combination as a first approximation. Measured peak areas (Table 3) agree fairly well with predictions made using the assumption of random distribution and these assignments (Table 3). High-level theoretical calculations, which have recently been demonstrated for predictions of shifts in paramagnetic phosphates,[37−42] could in the future help to confirm such assignments and relate them to quantitative variations in local structure.

One alternative explanation for the splitting observed here is that the "extra" peaks between −30 and −45 ppm are from ^{31}P nuclei with three Ce^{3+} neighbors. Such hypothetical triply shifted peaks would probably be combinations of peaks A and D along with one further contribution from peak B, C, E, or F. This explanation, however, is much less likely considering the predicted intensities of such peaks (Table 3). The observed intensities of peaks AD1, AD2, and AD3 are orders of magnitude greater than predicted intensities. Given the close agreement of the intensities of singly and doubly shifted peaks with a random distribution model, it is unlikely that any sort of deviation from this model could cause such a significant increase in the intensities of triply shifted peaks, and therefore, we find the invocation of triply shifted peaks to be highly improbable.

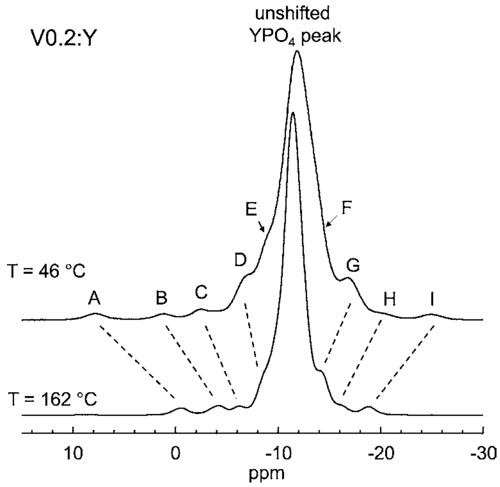

Figure 10. ^{31}P MAS NMR spectra of V0.2:Y ($Y_{1-x}V_xPO_4$, $x = 0.002$) collected with pulse delays of 1 s at temperatures of 46 °C (upper spectrum) and 162 °C (lower spectrum) illustrating the temperature dependence of paramagnetically shifted peak positions, as marked by dashed lines. Spectra are normalized to the maximum intensity.

$Y_{1-x}V_xPO_4$ Xenotime Solid Solution. The ^{31}P NMR spectra at 47 and 162 °C of flux-grown sample V0.2:Y (YPO_4 with 0.2% V, Table 1) are shown in Figure 10. In addition to the main unshifted peak at −11.4 ppm, there are at least nine low intensity peaks between −25 and +8 ppm, labeled A through I. The results of spectral decomposition are shown in Table 2. All of these features move in toward the main peak with increasing temperature, confirming their shifts as paramagnetic. Vanadium can have multiple possible oxidation states when substituting into inorganic materials. Considering solely ionic charge balance, the two most likely valences for V in YPO_4 are V^{5+} substituted for P^{5+} and V^{3+} for Y^{3+}. YVO_4 (V^{5+}) is a known compound and has found use as a laser or phosphor material when doped with either Nd^{3+} or Eu^{3+}, respectively.[44,45] Furthermore, the existence of a complete solid solution between YPO_4 and YVO_4 has been demonstrated.[46] However, V^{5+} has the [Ar] $3d^0$ electronic configuration and is diamagnetic, whereas V^{2+}, V^{3+}, and V^{4+} have [Ar] $3d^3$, [Ar] $3d^2$, and [Ar] $3d^1$, respectively, and are paramagnetic. EPMA analysis of this sample did not show a significant amount of any paramagnetic REE and, furthermore, the observed spectrum does not resemble those we describe here or previously[29] for REE-doped YPO_4. We therefore conclude that at least some of the vanadium in V0.2:Y is present as V^{2+}, V^{3+}, or V^{4+} substituting for Y^{3+}. Making peak assignments to specific $^{31}P{-}V$ configurations for this material is probably not possible at this point without knowing the valence of V. We can, however, make an estimate of the relative amount of paramagnetic V if we use a tentative peak assignment where each paramagnetically shifted peak is caused by sets of four symmetrically equivalent $^{31}P{-}V$ configurations as with peak A in the $Y_{1-x}REE_xPO_4$ materials described above. Then, the concentration of V in atoms per formula unit, x, is given by $x = I/4$, where I is the relative intensity of a paramagnetically shifted peak. The average value of the shifted peak areas was measured to be 0.7% utilizing A through I, but excluding the E and F, as their major overlap with the main unshifted peak made fitting imprecise. This gives a concentration of 0.18% for V, which is close to the total vanadium concentration given by EPMA (0.2 ± 0.1%), indicating that most of the V in this sample is present not as diamagnetic V^{5+} but as V^{2+}, V^{3+}, V^{4+}, or some combination of the three. Although the existence of a solid solution between YPO_4 and V^{5+}-bearing YVO_4 has been demonstrated,[44,45,47] it is possible that near the YPO_4 end member in the solid solution, strict adherence to the $YP_{1-x}V^{5+}{}_xO_4$ join is not followed. The oxidation state of a transition metal substituent such as V may also depend on the synthesis conditions and method.

■ CONCLUSIONS

The 100% natural abundance of ^{31}P and its high NMR sensitivity make phosphorus-bearing systems potentially rich in information regarding minor substitutional constituents and their bearing on solid solution mechanisms. Solid solutions composed of a paramagnetic component in a host diamagnetic phase may offer especially clear structural details relative to solid solutions containing only diamagnetic or only paramagnetic cations: the former because of the greater range of paramagnetic shifts relative to chemical shifts and thus greater separation and resolution of distinct resonances, and the latter because of the narrower line widths with lower concentrations of paramagnetic species.

In this study, we have demonstrated that ^{31}P MAS NMR provides strong evidence of random cation distributions in the $La_{1-x}Ce_xPO_4$ monazites and $Y_{1-x}M_xPO_4$ (M = Ce^{3+}, Nd^{3+}) xenotimes. In the monazites, a fully disordered distribution of La^{3+} and Ce^{3+} over the single crystallographic REE-O_9 site is based on modeling of spectra with peaks related to PO_4 tetrahedra having zero, one, two, three, or four nearest neighboring Ce^{3+} using a binomial distribution to predict intensities. For the xenotimes, evidence for the random distribution of Y^{3+} and Ce^{3+} or Nd^{3+} derives from the direct observation and quantification of peaks related to PO_4 tetrahedra having zero, one, or two paramagnetic neighbors and comparison to predictions of a random distribution model.

In addition to the information obtained concerning cation order/disorder in these systems, observations of deviations from linear additivity of paramagnetic shifts and of the splitting of some peaks strongly suggest local structural distortions caused by the substitution of the larger ions of Ce^{3+} (1.143 Å) or Nd^{3+} (1.109 Å) for Y^{3+} (1.019 Å).[2] Because paramagnetic shifts are typically rather large, any slight deviation in local structure can potentially lead to changes in peak positions that are small in proportion to the total shift but are large enough to be resolvable in an NMR experiment of sufficient resolution. Note that the magnitude of these effects increases with increasing cation size from Nd^{3+}, where the proposed structural distortion is manifested as slight splitting of one of the paramagnetically shifted peaks but linear shift additivity is largely observed, to Ce^{3+} wherein peak splitting and extreme deviations from shift additivity are observed.

The approach described in this paper has the potential to provide information on other systems. Of particular interest could be solid solutions between end members having different symmetries, such as the $Y_{1-x}LREE_xPO_4$ xenotime/monazites, but which have greater mutual solubilities than the binaries considered in this work. The relatively low amount of Ce^{3+} or Nd^{3+} that could be substituted into the YPO_4 lattice precludes the possibility of observing triply or quadruply shifted NMR resonances. If deviations from random cation distributions (e.g., clustering) are to be expected, they may become important, and more readily detectable, when the two structurally dissimilar end members are mixed together in more equal proportions, allowing more strain to build up in the crystal lattice. Observation of paramagnetically shifted NMR peaks and careful analysis and quantification of peak areas has the potential to provide a deeper level of understanding of solid solution mechanisms in many inorganic crystalline systems.

AUTHOR INFORMATION

Corresponding Author

*A. C. Palke. E-mail: apalke@stanford.edu.

Author Contributions

The manuscript was written through contributions of all authors. All authors have given approval to the final version of the manuscript.

Notes

The authors declare no competing financial interest.

ACKNOWLEDGMENTS

This research was supported by NSF grant EAR-1019596 to J.F.S. We thank Professor Robert Feigelson for helpful initial discussions and Bob Jones (Stanford) and Sarah Roeske and Nick Botto (University of California, Davis) for assistance with EPMA analyses. Research at the Oak Ridge National Laboratory for one author (L.A.B.) is sponsored by the U.S. Department of Energy, Basic Energy Sciences, Materials Sciences and Engineering Division.

REFERENCES

(1) Ni, Y.; Hughes, J. M.; Mariano, A. N. *Am. Mineral.* **1995**, *80*, 21–26.

(2) Shannon, R. D. *Acta Crystallogr., Sect. A: Cryst. Phys., Diffr., Theor. Gen. Crystallogr.* **1976**, *A32*, 751–767.

(3) Pyle, J. M.; Spear, F. S.; Rudnick, R. L.; McDonough, W. F. *J. Petrol.* **2001**, *42*, 2083–2107.

(4) Clavier, N.; Podor, R.; Dacheux, N. *J. Eur. Ceram. Soc.* **2011**, *31*, 941–976.

(5) Sales, B. C.; White, C. W.; Boatner, L. A. *Nucl. Chem. Waste Manage.* **1983**, *4*, 281–289.

(6) Boatner, L. A.; Abraham, M. M.; Sales, B. C. *Inorg. Chim. Acta* **1984**, *94*, 146–148.

(7) Boatner, L. A.; Sales, B. C. Monazite. In *Radioactive waste forms for the future*; Lutze, W., Ewing, R. C., Eds.; Elsevier Science: Amsterdam, 1988; pp 495–564.

(8) Meldrum, A.; Boatner, L. A.; Ewing, R. C. *Phys. Rev. B: Condens. Matter Mater. Phys.* **1997**, *56*, 13805–13814.

(9) Meldrum, A.; Boatner, L. A.; Weber, W. J.; Ewing, R. C. *Geochim. Cosmochim. Acta* **1998**, *62*, 2509–2520.

(10) Meldrum, A.; Boatner, L. A.; Ewing, R. C. *Mineral. Mag.* **2000**, *64*, 185–194.

(11) Oelkers, E. H.; Montel, J.-M. *Elements* **2008**, *4*, 113–116.

(12) Dacheux, N.; Clavier, N.; Podor, R. *Am. Mineral.* **2013**, *98*, 833–847.

(13) Williams, M. L.; Jercinovic, M. J.; Hetherington, C. J. *Annu. Rev. Earth Planet. Sci.* **2007**, *35*, 137–175.

(14) Catlos, E. J. *Am. Mineral.* **2013**, *98*, 819–832.

(15) MacKenzie, K. J. D.; Smith, M. E. *Multinuclear Solid-State Nuclear Magnetic Resonance of Inorganic Materials*; Elsevier: Oxford, U.K., 2002; Vol. *6*.

(16) Kim, J.; Nielsen, U. G.; Grey, C. P. *J. Am. Chem. Soc.* **2008**, *130*, 1285–1295.

(17) Nielsen, U. G.; Majzlan, J.; Grey, C. P. *Chem. Mater.* **2008**, *20*, 2234–2241.

(18) Cabana, J.; Shirakawa, J.; Chen, G.; Richardson, T. J.; Grey, C. P. *Chem. Mater.* **2010**, *22*, 1249–1262.

(19) Bose, M.; Bhattacharya, M.; Ganguli, S. *Phys. Rev. B: Condens. Matter Mater. Phys.* **1979**, *19*, 72–80.

(20) Bregiroux, D.; Audubert, F.; Charpentier, T.; Sakellariou, D.; Bernache-Assollant, D. *Solid State Sci.* **2007**, *9*, 432–439.

(21) Lee, Y. J.; Park, S.-H.; Eng, C.; Parise, J. B.; Grey, C. P. *Chem. Mater.* **2001**, *14*, 194–205.

(22) Yoon, W. S.; Iannopollo, S.; Grey, C. P.; Carlier, D.; Gorman, J.; Reed, J.; Ceder, G. *Electrochem. Solid-State Lett.* **2004**, *7*, A167–A171.

(23) Meng, Y. S.; Ceder, G.; Grey, C. P.; Yoon, W. S.; Jiang, M.; Bréger, J.; Shao-Horn, Y. *Chem. Mater.* **2005**, *17*, 2386–2394.

(24) Bréger, J.; Dupré, N.; Chupas, P. J.; Lee, P. L.; Proffen, T.; Parise, J. B.; Grey, C. P. *J. Am. Chem. Soc.* **2005a**, *127*, 7529–7537.

(25) Bréger, J.; Jiang, M.; Dupré, N.; Meng, Y. S.; Shao-Horn, Y.; Ceder, G.; Grey, C. P. *J. Solid State Chem.* **2005b**, *178*, 2575–2585.

(26) Zeng, D.; Cabana, J.; Bréger, J.; Yoon, W.-S.; Grey, C. P. *Chem. Mater.* **2007**, *19*, 6277–6289.

(27) Palke, A. C.; Stebbins, J. F.; Frost, D. J.; McCammon, C. A. *Am. Mineral.* **2012**, *97*, 1955–1964.

(28) Pourpoint, F. d. r.; Hua, X.; Middlemiss, D. S.; Adamson, P.; Wang, D.; Bruce, P. G.; Grey, C. P. *Chem. Mater.* **2012**, *24*, 2880−2893.

(29) Palke, A. C.; Stebbins, J. F. *Am. Mineral.* **2011a**, *96*, 1343−1353.

(30) Feigelson, R. S. *J. Am. Ceram. Soc.* **1964**, *47*, 257−258.

(31) Boatner, L. A.; Sales, B. C. Monazite. In *Radioactive waste forms for the future*; Lutze, W., Ewing, R. C., Eds.; Elsevier Science: Amsterdam, 1988; pp 495−564.

(32) Takahashi, T.; Kawashima, H.; Sugisawa, H.; Toshihide, B. *Solid State Nucl. Magn. Reson.* **1999**, *15*, 119−123.

(33) Frye, J. S.; Maciel, G. E. *J. Magn. Reson.* **1982**, *48*, 125−131.

(34) Massiot, D.; Fayon, F.; Capron, M.; King, I.; Le Calvé, S.; Alonso, B.; Durand, J.-O.; Bujoli, B.; Gan, Z.; Hoatson, G. *Magn. Reson. Chem.* **2002**, *40*, 70−76.

(35) Grey, C. P.; Dobson, C. M.; Cheetham, A. K.; Jakeman, R. J. B. *J. Am. Chem. Soc.* **1989**, *111*, 505−511.

(36) Palke, A. C.; Stebbins, J. F. *Am. Mineral.* **2011b**, *96*, 1090−1099.

(37) Carlier, D.; Ménétrier, M.; Grey, C. P.; Delmas, C.; Ceder, G. *Phys. Rev. B: Condens. Matter Mater. Phys.* **2003**, *67*, 174103.

(38) Yoon, W. S.; Iannopollo, S.; Grey, C. P.; Carlier, D.; Gorman, J.; Reed, J.; Ceder, G. *Electrochem. Solid-State Lett.* **2004**, *7*, A167−A171.

(39) Kim, J.; Middlemiss, D. S.; Chernova, N. A.; Zhu, B. Y. X.; Masquelier, C.; Grey, C. P. *J. Am. Chem. Soc.* **2010**, *132*, 16825−16840.

(40) Clément, R. l. J.; Pell, A. J.; Middlemiss, D. S.; Strobridge, F. C.; Miller, J. K.; Whittingham, M. S.; Emsley, L.; Grey, C. P.; Pintacuda, G. *J. Am. Chem. Soc.* **2012**, *134*, 17178−17185.

(41) Pourpoint, F. d. r.; Hua, X.; Middlemiss, D. S.; Adamson, P.; Wang, D.; Bruce, P. G.; Grey, C. P. *Chem. Mater.* **2012**, *24*, 2880−2893.

(42) Middlemiss, D. S.; Ilott, A. J.; Clement, R. J.; Strobridge, F. C.; Grey, C. P. *Chem. Mater.* **2013**, *25*, 1723−1734.

(43) Bakhmutov, V. I. *Practical NMR Relaxation for Chemists*; Wiley: West Sussex, U.K., 2004.

(44) Zhu, H.; Yang, H.; Jin, D.; Wang, Z.; Gu, X.; Yao, X.; Yao, K. *J. Nanopart. Res.* **2008**, *10*, 1149−1154.

(45) Zhu, H.; Zuo, D. *J. Phys. Chem. C* **2009**, *113*, 10402−10406.

(46) Ladwig, G.; Jost, K.-H.; Schlesinger, K. *Z. Chem. (Stuttgart, Ger.)* **1979**, *19*, 386−386.

(47) Ropp, R. C.; Carroll, B. *Inorg. Chem.* **1975**, *14*, 2199−2202.